

## Article

# High-Sensitivity Sensor Based on Diametrical Graphene Strip Plasma-Induced Transparency

Aijun Zhu <sup>1,2,3</sup> , Pengcheng Bu <sup>1</sup>, Lei Cheng <sup>3,4,\*</sup>, Cong Hu <sup>1</sup> and Rabi Mahapatra <sup>5</sup>

<sup>1</sup> School of Electronic Engineering and Automation, Guilin University of Electronic Technology, Guilin 541004, China; zbluebird@guet.edu.cn (A.Z.); 21082304003@mails.guet.edu.cn (P.B.); hucong@guet.edu.cn (C.H.)

<sup>2</sup> Guangxi Key Laboratory of Automatic Detecting Technology and Instruments, Guilin 541004, China  
<sup>3</sup> Shanxi Key Laboratory of Advanced Semiconductor Optoelectronic Devices and Integrated Systems, Jincheng 048000, China

<sup>4</sup> Jincheng Research Institute of Opto-Mechatronics Industry, Jincheng 048000, China

<sup>5</sup> Department of Computer Science and Engineering, Texas A&M University, College Station, TX 77843-3112, USA; rabi@tamu.edu

\* Correspondence: chenglei@jcgjd.org.cn

**Abstract:** In this paper, two parallel graphene strip structures are adopted to achieve tunable plasma-induced transparency (PIT) sensors in the terahertz band. Both graphene bands act as bright modes, and a PIT window appears due to the weak hybridization between them. A Lorentzian oscillation coupling model is fitted to the simulation results of the proposed structure by the finite-difference time-domain (FDTD) method and is in good agreement with the simulation results. The performance of the PIT system can be controlled by tuning the geometrical parameters of the structure. In addition, the resonant frequency of the PIT window can be dynamically adjusted by changing the chemical potential and carrier mobility of the graphene strips. When the chemical potential of graphene increases from 0.2 eV to 1 eV, the amplitude modulation depth of the PIT window (2.832 THz, 3.684 THz, and 4.386 THz) can reach 92.39%, 96.14%, and 90.4%, respectively. Furthermore, due to its dispersion characteristics, the realized PIT window has a sensitive response to the surrounding medium, and the sensitivity can be as high as 1.25 THz/RIU. This PIT effect-based graphene microstructure has important implications for the future design of terahertz modulators, optical switches, and ultrasensitive sensors.



**Citation:** Zhu, A.; Bu, P.; Cheng, L.; Hu, C.; Mahapatra, R.

High-Sensitivity Sensor Based on Diametrical Graphene Strip Plasma-Induced Transparency.

*Photonics* **2023**, *10*, 830. <https://doi.org/10.3390/photonics10070830>

Received: 26 June 2023

Revised: 12 July 2023

Accepted: 14 July 2023

Published: 17 July 2023



**Copyright:** © 2023 by the authors. Licensee MDPI, Basel, Switzerland. This article is an open access article distributed under the terms and conditions of the Creative Commons Attribution (CC BY) license (<https://creativecommons.org/licenses/by/4.0/>).

**Keywords:** graphene; plasma-induced transparency; the finite-difference time-domain; high sensitivity

## 1. Introduction

Electronically induced transparency (EIT) is a quantum interference effect that occurs in three-energy atomic systems and produces sharp windows of transparency within a broad absorption spectrum [1,2]. However, the research and practical applications of EIT in atomic systems are greatly limited by specific experimental conditions such as low temperature, coherent pumping, and high intensity [3]. To solve this problem, many researchers have endeavored to model the classical EIT effect in a new way. Surface plasmon polaritons (SPPs) supported at the metal–dielectric interface have the ability to confine electromagnetic waves in the subwavelength range and overcome the classical diffraction limit [4,5]. Therefore, plasma-induced transparency (PIT), an optical effect similar to EIT, has attracted much attention due to its remarkable advantages and wide practical applications [6]. In general, there are two schemes to achieve PIT: bright–dark mode coupling (direct coupling) [7–11] and bright–bright mode coupling (indirect coupling) [12–16]. Unlike the first approach, which is based on the phase extinction interference between the bright and dark modes, the second approach stems from the detuning between the bright and light modes, which has attracted the attention of an increasing number of researchers. In recent years, structures

formed by conventional metallic materials such as Al, Cu, Ag, Au, etc. with dielectric layer materials are also capable of forming PIT window phenomena [17–19]. However, these aforementioned structures composed of metallic materials have huge propagation losses, making it difficult to control the dielectric constants of the metals, which will result in low modulation ranges. Changing the geometrical parameters of the conventional metallic material pattern layers to achieve dynamic control of the PIT window is essential, but the possibility of large-scale remanufacturing is still limited by the complex structures and processes, making it difficult to use widely. Moreover, it is inconvenient to adjust the geometric parameters of the metallic material pattern layer once the device is fabricated. Meanwhile, this method has the obvious drawback that the PIT peak is shifted as the structure is adjusted, which hinders the practical application effect of bright–bright mode coupled PIT in filters and modulators [20–22]. To address this problem, graphene, an emerging two-dimensional material composed of honeycomb carbon atoms, has been proposed to design tunable PIT devices because its plasmonic response can be actively tuned by a controlled graphene chemical potential [23–26]. Due to their superior optical properties, including flexible tunability, tight field confinement, and low propagation loss [27–29], various graphene-based PIT devices, such as graphene–metal hybrid structures [30,31], multilayer graphene structures [32–34], and graphene-based substructures [35,36], have been widely studied to tune the PIT effect. Compared to the complex structure of patterned graphene rings with multiple PIT window effects [37–39], our proposed structure is not only simple, but also obtains a higher sensitivity. Therefore, it has a greater potential to be widely used in practical applications. Furthermore, it is possible to analyze the effect of different graphene nanoribbon parameters (e.g., length, width, intermediate distance, position, etc.) [40,41].

In this paper, we design a 2D graphene metamaterial structure to achieve the PIT effect at terahertz frequencies. The structure consists of two parallel graphene strips. Compared with the above structures, it is very simple and easy to fabricate this metamaterial structure. By analyzing the surface electric field distribution of the transmission peak, weak hybridization between two bright modes with frequency detuning produces a PIT optical response in the terahertz region. The FDTD simulation results of the proposed structure are in high agreement with the theoretical calculations of the Lorentzian oscillation coupling model. Meanwhile, the effects of structural parameters on the PIT, such as the length and width of each of the two graphene strips, the distance between the two strips, and the carrier mobility of graphene, were investigated. In addition, the maximum modulation depth of the PIT window can reach 96.14% by changing the chemical potential of graphene. Furthermore, the proposed graphene microstructure also has an extremely high sensitivity of 1.25 THz/RIU to the variation of the surrounding medium. The sensing performance is greatly improved compared to the recently reported metamaterial sensors based on the PIT effect in the terahertz region.

## 2. Metamaterial Structure and FDTD Simulation Model

Figure 1a shows a schematic view of the proposed graphene metamaterial structure. The polarization angle  $\theta$  is the angle between the electric field polarization direction and the  $x$ -axis. From the figure, it can be observed that the graphene microstructure consists of two parallel graphene strips and a Si substrate array cell periodically. The length  $L$ , thickness, and index of the Si substrate in Figure 1b are 4  $\mu\text{m}$ , 0.15  $\mu\text{m}$ , and 3.42, respectively. The length and width of the long graphene strip (strip1) are  $L_1$  and  $W_1$ , respectively. The length and width of the short graphene strip (strip2) are  $L_2$  and  $W_2$ , respectively. The distance between two parallel graphene strips is  $S$ . In the final fabrication of graphene metamaterials, we can lay an ionic gel layer on top of the graphene pattern layer by mechanical spin coating and deposit gold grid contacts above the ionic gel layer and below the substrate. Since the ultra-thin ionic gel layer has little effect on the spectrum as an electrode medium, it can be neglected in the simulation. When we change the gate voltage, the chemical potential of graphene can be changed by the ionic gel layer, and, finally, the

dynamic regulation of graphene conductivity is achieved [39]. In this paper, a full-wave numerical simulation of the transmission spectrum of this system is performed using the FDTD method. In order to balance the simulation time and accuracy, a suitable grid is used during the simulation calculations. Periodic boundary conditions are applied in the x and y directions, and perfectly matched layers are placed along the incident plane of light in the z direction.

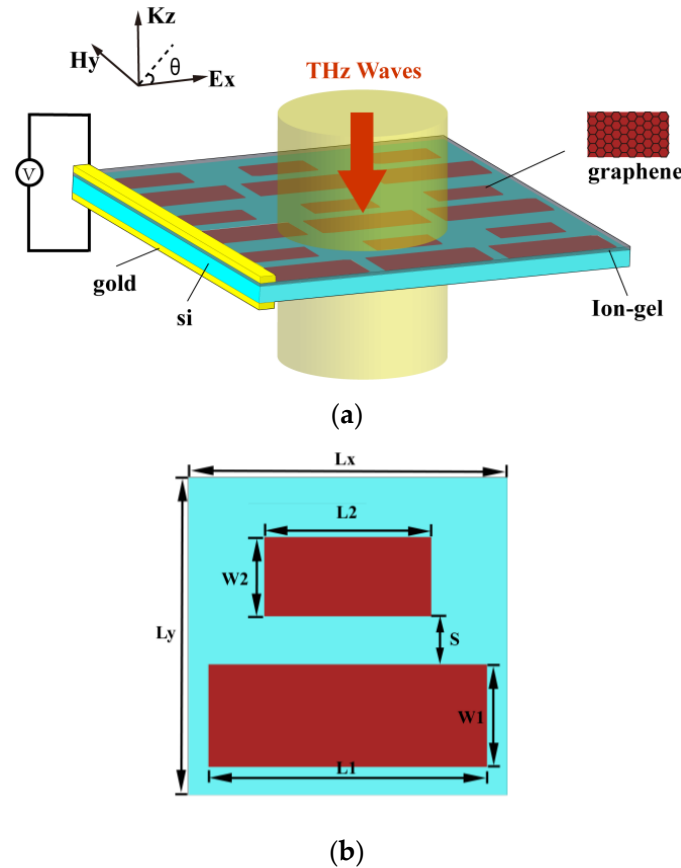


**Figure 1.** (a) Schematic view of the proposed graphene metamaterial in stereo. (b) Top view of the cell of the graphene metamaterial structure with geometric parameters.

According to the Kubo model of conductivity of monolayer graphene, the optical properties of graphene depend on the angular frequency  $\omega$ , the scattering rate  $\Gamma$ , the chemical potential  $\mu_c$ , and the temperature  $T$ . Its conductivity consists of two components, intraband electron–photon scattering and direct interband electron leap, as follows [42]:

$$\sigma(\omega, \Gamma, \mu_c, T) = \sigma_{inter}(\omega, \Gamma, \mu_c, T) + \sigma_{intra}(\omega, \Gamma, \mu_c, T) \tag{1}$$

$$\sigma_{inter} = \frac{ie^2}{4\pi\hbar} \ln \frac{2|\mu_c| - (\omega + i2\Gamma)\hbar}{2|\mu_c| + (\omega + i2\Gamma)\hbar} \tag{2}$$

$$\sigma_{intra} = \frac{ie^2k_B T}{\pi\hbar^2(\omega + i2\Gamma)} \left[ \frac{\mu_c}{k_B T} + 2 \ln \left( 1 + e^{-\frac{\mu_c}{k_B T}} \right) \right] \tag{3}$$

where  $e$  is the electron charge,  $\hbar$  is the approximate Planck constant, and  $k_B$  is the Boltzmann constant. The scattering rate is related to the electron relaxation time ( $\tau$ ) through  $2\Gamma = \tau^{-1}$ . In the terahertz range, the direct interband electron jumps can be neglected due to  $|\mu_c| \gg \hbar\omega/2$ , so the conductivity of monolayer graphene is mainly generated by intraband electron–photon scattering. In our proposed system, the temperature  $T$  is set to

300 K, which leads to  $k_B T \ll \mu_c$ . Thus, the conductivity of monolayer graphene can be similar to the metallic Drude expressions [43,44], as follows:

$$\sigma_g = \frac{ie^2\mu_c}{\pi\hbar^2(\omega + i2\Gamma)} \tag{4}$$

To further analyze the properties of graphene, its propagation constant needs to be calculated. The propagation constant  $\beta$  and the effective refractive index  $n_{eff}$  of the conducting mode can be expressed as follows [45,46]:

$$\beta = k_0 \sqrt{\epsilon_1 - \left(\frac{2\epsilon_1}{\eta_0\sigma_g}\right)^2} \tag{5}$$

$$n_{eff} = \frac{\beta}{k_0} \tag{6}$$

Here,  $k_0$  is the wave number in free space,  $\eta_0$  is the intrinsic impedance, and  $\epsilon_1$  is the relative dielectric constant of dielectric silicon. Therefore, we can calculate the real and imaginary parts of the effective refractive index with frequency from Equation (6), as shown in Figure 2.

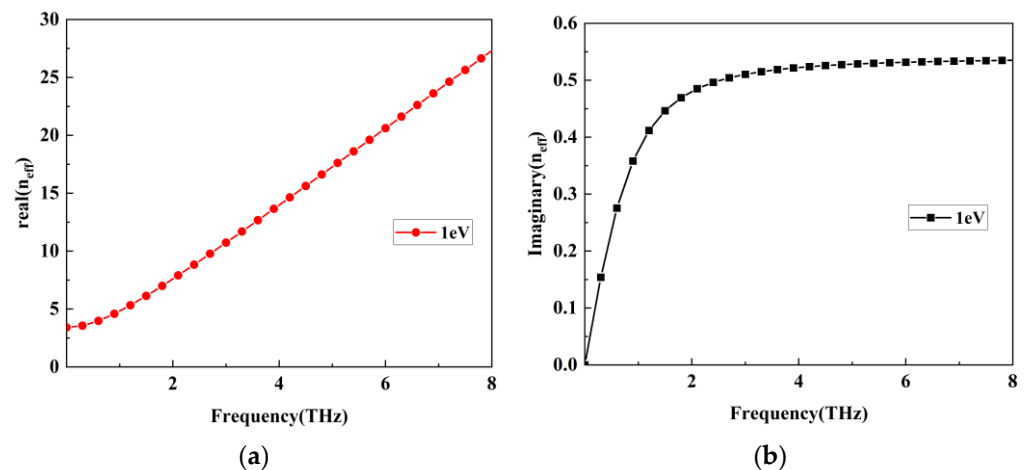


**Figure 2.** (a) When  $\mu_c = 1$  eV, the real part of the effective refractive index varies with frequency. (b) When  $\mu_c = 1$  eV, the imaginary part of the effective refractive index varies with frequency.

### 3. Results and Discussion

To investigate the mechanism of inducing transparent windows in the proposed metamaterial structure, we numerically calculated the transmission spectra along the x-polarization direction. We discuss the simulation results for the structure of the cell in Figure 3. Apparently, the two graphene strips in Figure 3a produce a single PIT peak window plotted with red lines at 4.68 THz. In order to understand the formation process of the PIT, we need to understand the contribution of each part. In particular, the black line in Figure 3a represents the bright mode contributed by the short graphene strip (strip2), and the blue line represents the bright mode contributed by the long graphene strip (strip1). Due to the mode interactions in the proposed structure, PIT valleys associated with the two dips are obtained at 3.63 THz and 5.61 THz, with a transmission of 0.88 at 4.68 THz.

The z-component electric field distributions of the two transmission dips (3.63 and 5.61 THz) and the transmission peak (4.68 THz) are shown in Figure 3b–d, which further contribute to the understanding of the PIT effect obtained through bright–bright mode coupling. As can be seen in Figure 3b, corresponding to the dip at 3.63 THz, only strip1 is strongly excited by the incident light due to the interference effect between strip1 and strip2, but the field intensity around strip2 is very weak. In contrast, in Figure 3c, the

field distribution of strip1 and strip2 bands at 5.61 THz is completely opposite to that in Figure 3b. When the 4.68 THz frequency is applied in Figure 3d, the two graphene strips are excited simultaneously due to resonance detuning. At the same time, the phases of two strips at the same end are opposite.

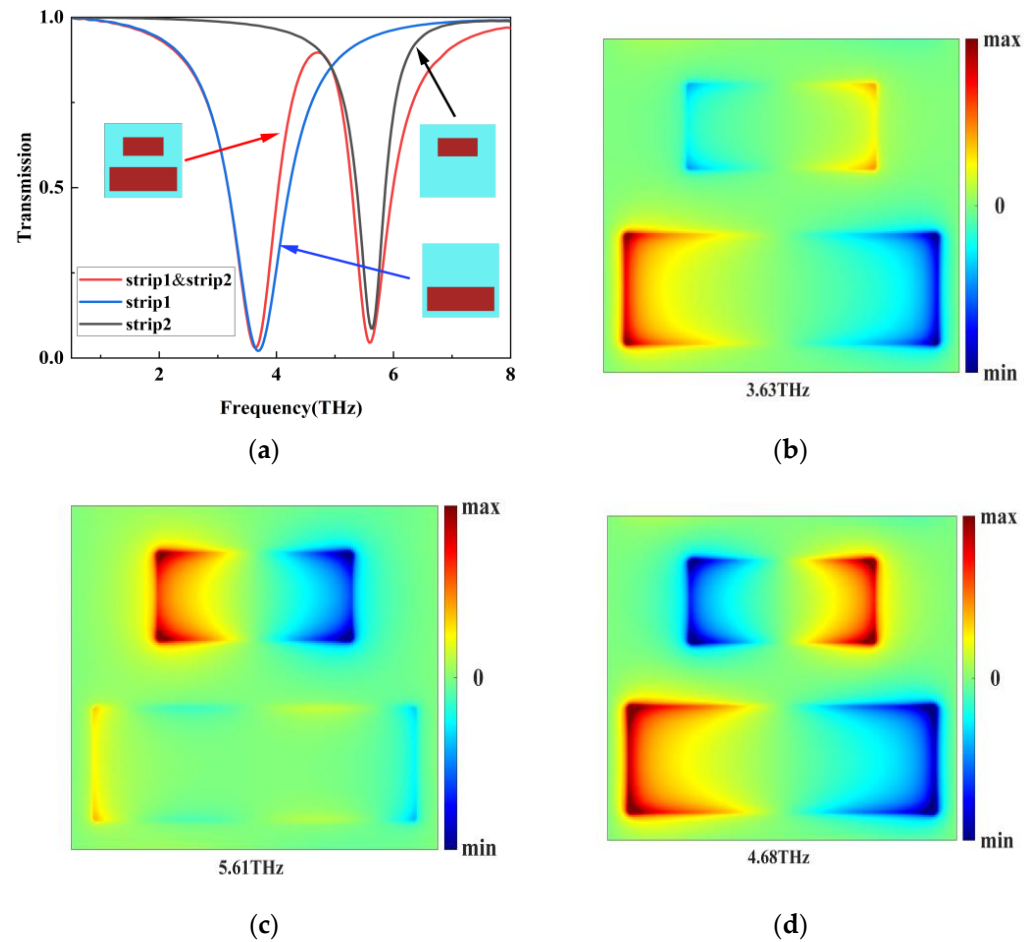


**Figure 3.** (a) Z-directional distribution of the normalized electric field in the structure proposed in the transmission spectra (b–d) of a single PIT excitation process at frequencies of 3.63, 4.68, and 5.61 THz, respectively, when  $\mu_c = 1$  eV.

To better illustrate the formation process of the PIT transparent window, we use the Lorentz oscillatory coupling model to fit the parameters to the FDTD simulation results. In the coupling model, the incident plane wave is denoted by  $\tilde{E}(\omega)e^{i\omega t}$ , the bright mode 1 resonator by  $\tilde{M}_1(\omega)e^{i\omega t}$ , and the bright mode 2 resonator by  $\tilde{M}_2(\omega)e^{i\omega t}$ . By definition, the Lorentz oscillatory coupling model under bright-mode coupling can be expressed as [47,48]:

$$\begin{bmatrix} \omega - \omega_1 + i\gamma_1 & \tilde{k} \\ \tilde{k} & \omega - \omega_2 + i\gamma_2 \end{bmatrix} \begin{bmatrix} \tilde{M}_1 \\ \tilde{M}_2 \end{bmatrix} = \begin{bmatrix} g_1 \tilde{E} \\ g_2 \tilde{E} \end{bmatrix} \quad (7)$$

where  $\omega_1, \omega_2, \gamma_1, \gamma_2$  represent the resonant frequencies and damping factors of bright mode 1 and bright mode 2, respectively;  $\tilde{k}$  represents the coupling coefficient between the two bright modes;  $g_1$  represents the coupling strength between bright mode 1 and the electromagnetic field; and  $g_2$  represents the coupling strength between bright mode 2 and the electromagnetic field.

Since the energy dissipation of the metamaterial structure is mainly determined by the imaginary part of the magnetic permeability, the transmittance of the graphene metamaterial structure can be simply expressed as [44]:

$$T(\omega) = 1 - \left| \frac{\tilde{M}_1}{\tilde{E}} \right|^2 = 1 - \left| \frac{(g_1(\omega - \omega_2 + i\gamma_2) - g_2\tilde{k})\tilde{E}}{(\omega - \omega_1 + i\gamma_1)(\omega - \omega_2 + i\gamma_2) - \tilde{k}^2} \right|^2 \quad (8)$$

By using the Lorentz oscillatory coupling model in Equation (8), we have numerically fitted the FDTD simulation transmission curves for the case of cell structure size  $L_x = L_y = 4 \mu\text{m}$ ,  $L_1 = 3.5 \mu\text{m}$ ,  $W_1 = 1.3 \mu\text{m}$ ,  $L_2 = 2.1 \mu\text{m}$ ,  $W_2 = 1 \mu\text{m}$ ,  $S = 0.4 \mu\text{m}$  in Figure 1b, as shown in Figure 4.

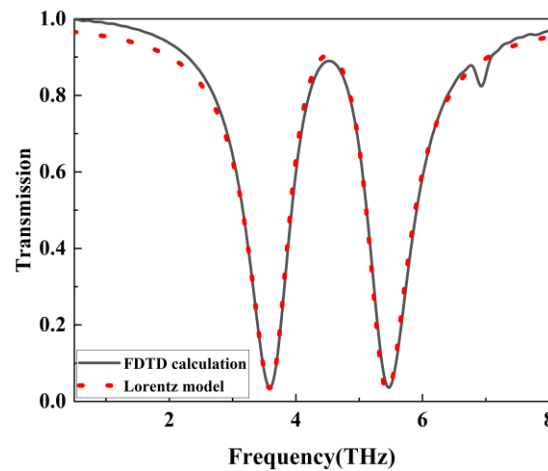
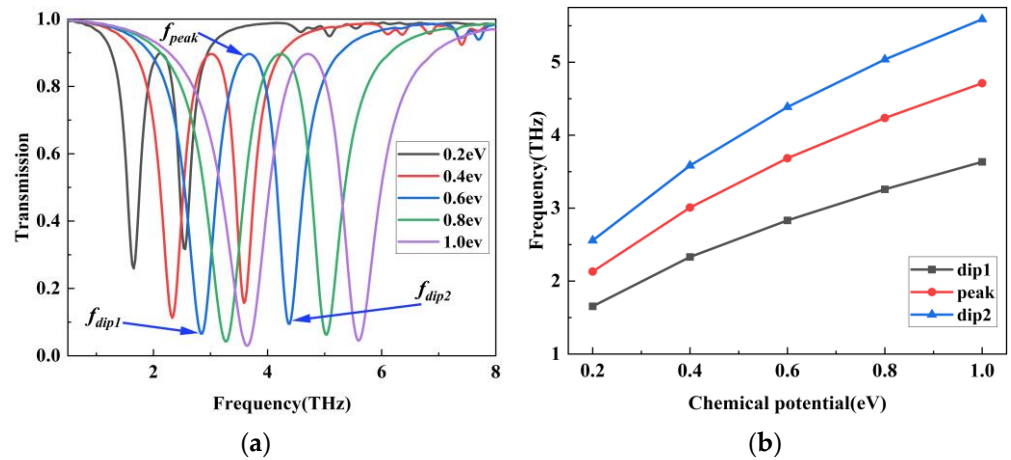


Figure 4. Fitting curve of Lorentz coupling model and FDTD simulation results.

The fitted parameters are as follows:  $\omega_1 = 5.39 \text{ THz}$ ,  $\omega_2 = 3.67 \text{ THz}$ ,  $g_1 = 0.714 \text{ THz}$ ,  $g_2 = 6.44 \text{ THz}$ ,  $k = 0.0941 \text{ THz}$ ,  $\gamma_1 = 0.396 \text{ THz}$ , and  $\gamma_2 = 0.389 \text{ THz}$ . As can be seen from Figure 4, the Lorentzian coupling model curves are in good agreement with the simulation results. Therefore, the reliability and accuracy of the PIT curve obtained from the FDTD simulation are further verified.

The proposed graphene metamaterial structure has a very typical PIT phenomenon. When the graphene chemical potential increases from 0.2 eV to 1.0 eV, the PIT transparent window not only has a significant blue shift but also satisfies the conclusion  $f \propto \sqrt{\frac{\alpha_0 c \mu_c}{2\pi^2 h L}}$ , where  $f$  is the resonant frequency of the microstructure,  $\alpha_0$  the structural constant, and  $L$  the length of the graphene cut line [49]. Meanwhile, the surface conductivity of the graphene metamaterial depends on its chemical potential, so the position of the PIT window can be effectively tuned by applying a bias voltage. The PIT effect will become obvious as the chemical potential increases. The amplitude modulation of the PIT window can be achieved by controlling the chemical potential of graphene. To evaluate the modulation performance of the metamaterial structure, a PIT window with  $\mu_c = 0.6 \text{ eV}$  was chosen as the study object. Three typical resonant frequencies of the PIT window were  $f_{dip1} = 2.832 \text{ THz}$ ,  $f_{peak} = 3.684 \text{ THz}$ , and  $f_{dip2} = 4.386 \text{ THz}$ . Figure 5b illustrates the variation of transmission peak and transmission dip with the chemical potential of graphene. The amplitude modulation performance at the three frequencies is analyzed by introducing the modulation depth  $M_D$ , defined as  $M_D = |T_{max} - T_{min}|/T_{max}$ , where  $T_{max}$  and  $T_{min}$  denote the maximum and minimum transmission amplitudes at the resonant frequencies, respectively. The modulation depth at the three resonant frequencies of  $f_{dip1}$ ,  $f_{peak}$ , and  $f_{dip2}$  can reach 92.39%, 96.14%, and 90.4%, respectively. On the other hand, the high and low transmission amplitude values can be set to 1 and 0 due to the large variation in

transmission amplitude at the three typical frequencies. The optical switch can be set to “on” or “off” by simply adjusting the chemical potential.



**Figure 5.** (a) Transmission spectrum of the PIT window with the variation of graphene chemical potential. (b) The variation of transmission peak and transmission dip with the chemical potential of graphene.

Then, we analyzed the effect of different carrier mobilities of graphene on the PIT window. It is well known that for graphene, higher carrier mobility can reduce the transmission loss and achieve higher transmittance in the transmission spectrum, as shown in Figure 6a. In addition, with the increase in carrier mobility, the plasma-induced transparent window has a red-shift phenomenon, as shown in Figure 6b.

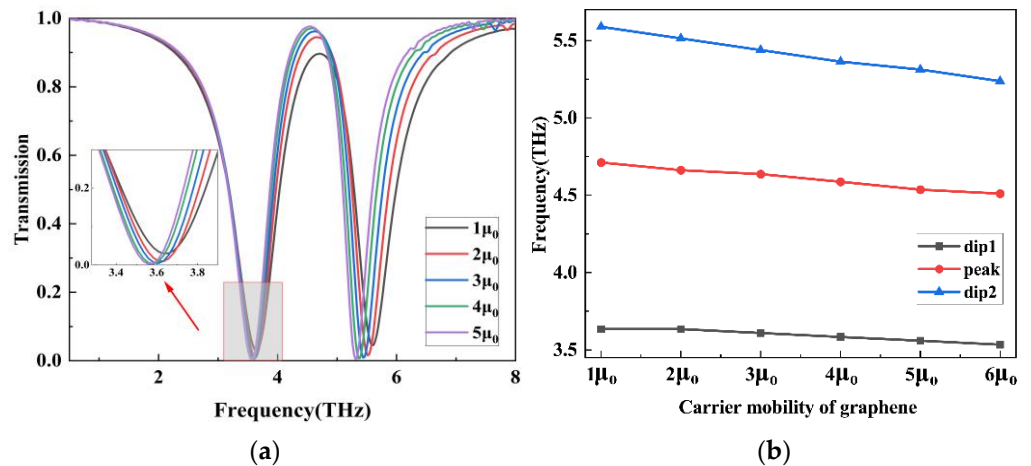


**Figure 6.** (a) Transmission spectrum of PIT window with carrier mobility. (b) The peak and trough values of transmission versus carrier mobility.

Moreover, as shown in Figure 7a,b, the effect of length L1 on the PIT window remains unchanged when L2, W2 and W1. Clearly, length L1 determines the coupling strength between the two graphene strips and the resonant frequency of bright mode 1. When the length of strip1 is around 3.5 μm, the induced electric field strength of the two graphene strips is almost equal, and frequency detuning can be easily achieved, which can lead to a more pronounced PIT window. When the difference between length L1 of strip1 and 3.5 μm is large, the difference between the induced electric field intensity of the two graphene strips increases, which leads to the deformation of the PIT window. Similarly, as shown in Figure 7c,d, the effect of length L2 on the PIT window remains unchanged when L1, W1, and W2 of strip2. The results of the analysis are similar to the effect of length L1 on the PIT window. Length L2 determines the coupling strength between the

two graphene strips and the resonant frequency of bright mode 2. The analysis shows that the resonant frequencies of the corresponding bright modes will be red-shifted as the lengths of strip1 and strip2 increase, respectively, while the peak value of the transmission spectrum of the corresponding PIT will increase and the dip value will decrease. Similarly, as shown in Figure 7e–h, we analyzed the effect of the widths W1 and W2 on the PIT window, respectively. The simulation results show that the PIT windows formed by weak hybridization of the two graphene strips are relatively stable when only the width W1 is changed. When only the width W2 is changed, the resonant frequency of the corresponding bright mode will be blue-shifted as the width W2 increases, and the peak value of the transmission spectrum of the corresponding PIT will increase and the dip value will decrease.

Next, we consider the effect of the distance S between two parallel graphene strips on the PIT window. Figure 8 shows the transmission spectral response of the proposed structure when the geometrical parameter S takes different values. From Figure 8a,b, it can be seen that there is no PIT effect when  $S = 0 \mu\text{m}$ . When S gradually increases, the PIT effect appears. The resonant frequencies of the bright modes corresponding to strip 1 and strip 2 will be blue-shifted, while the peak and dip2 values of the transmission spectrum of the corresponding PIT will increase and the dip1 value will decrease. Combining Figure 8a,b, it can be seen that the PIT phenomenon changes only slightly when the distance  $S > 0.6 \mu\text{m}$ . Therefore, parameter  $S > 0.6 \mu\text{m}$  has a minor effect on PIT. Interestingly, the Lorentzian oscillation coupling model fitting parameters are shown in Table 1. Results show that the resonant frequencies  $\omega_1$ ,  $\omega_2$ ,  $\gamma_1$ ,  $\gamma_2$ , and  $\tilde{k}$  in the theoretical model converge to stable values at  $S > 0.6 \mu\text{m}$ . Since the FDTD simulation calculations fit well with the Lorentzian oscillation coupling model, the convergence of the fitted parameter values indicates that a better transparency window is attributed to weaker hybridization [13] and that the Lorentzian oscillation coupling model can quantitatively describe the hybridization through the fitted parameters.

We also analyzed the sensitivity of the microstructure and calculated the variation of the transmission spectrum. As shown in Figure 9a, when the refractive index of the surrounding medium is increased from 1 to 1.5 with 0.1 intervals, the PIT window will show a significant redshift, and the position of the transmission peak moves from 4.712 THz to 4.085 THz. According to Figure 9b, the linear fit is consistent with the expectation between the frequency shift of the transmission peak and the refractive index. By fitting the curve, the sensitivity of the graphene metamaterial can be as high as 1.253 THz/RIU. Table 2 summarizes the performance of the graphene PIT system and compares it with previous studies that exploited the PIT effect [50–53]. It is noteworthy that the sensitivity values of the proposed structure are much higher than the results reported in recent studies. The results indicate that the proposed graphene structure is able to effectively sense changes in the refractive index of the environment. It has a reference value for the application of high-precision sensors in the terahertz region.

Figure 10a,b show the transmission spectra at different polarization angles varying from  $0^\circ$  to  $90^\circ$  with a step of  $20^\circ$ . When the incident light polarization angle is below  $60^\circ$ , we can see that the resonant frequencies do not change significantly, while the dip values of the transmission spectra of the corresponding PIT increase and the dip value changes significantly. The PIT window gradually disappears when the incident light polarization angle is greater than  $60^\circ$ . These analyses suggest that the proposed PIT graphene metamaterial structure is sensitive to the polarization angle because it is not highly symmetric. In Figure 10c,d, the incident angle varies with a step of  $10^\circ$  from  $0^\circ$  to  $60^\circ$ , and the spectrum changes slightly only when the incident angle approaches  $60^\circ$ . In summary, the sensor has a certain polarization angle and wide incidence angle insensitivity characteristics that can be applied to a complex test environment with large interference.

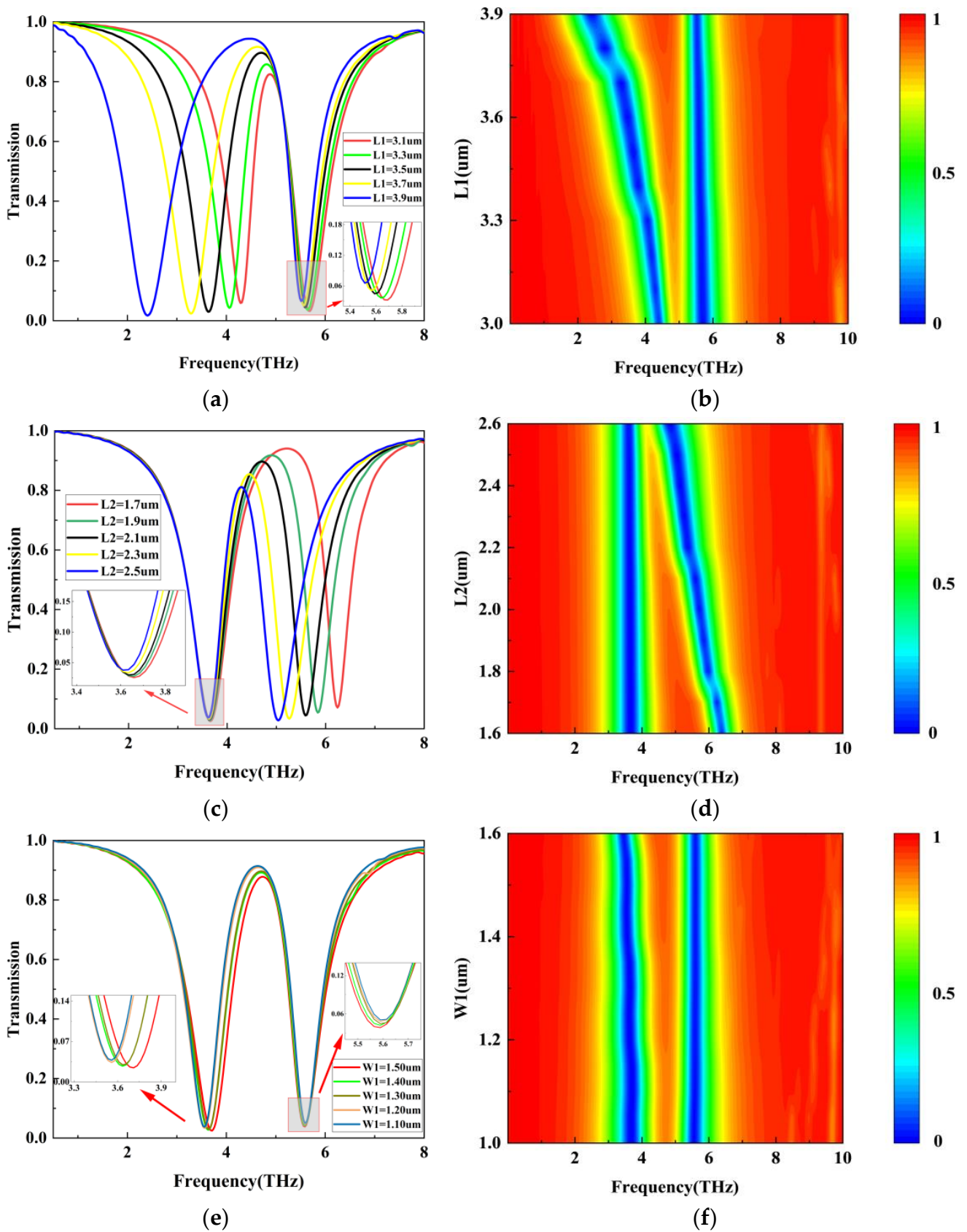


Figure 7. Cont.

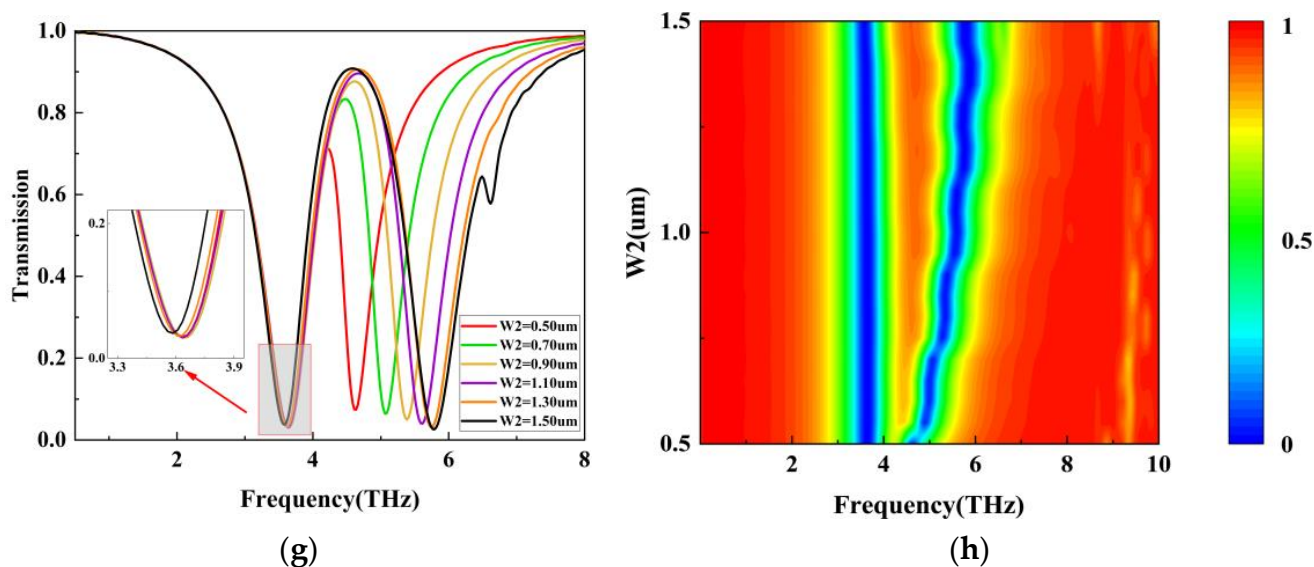


Figure 7. Transmission spectra of PIT windows for different cases (a) length of long transverse graphene strip (strip1)  $L_1$ , (c) length of short transverse graphene strip (strip2)  $L_2$ ; (e) width of long transverse graphene strip (strip1)  $W_1$ ; (g) width of short transverse graphene strip (strip2) of width  $W_2$ . Figures (b,d,f,h), show the corresponding transmission spectral isopleth maps for different cases.

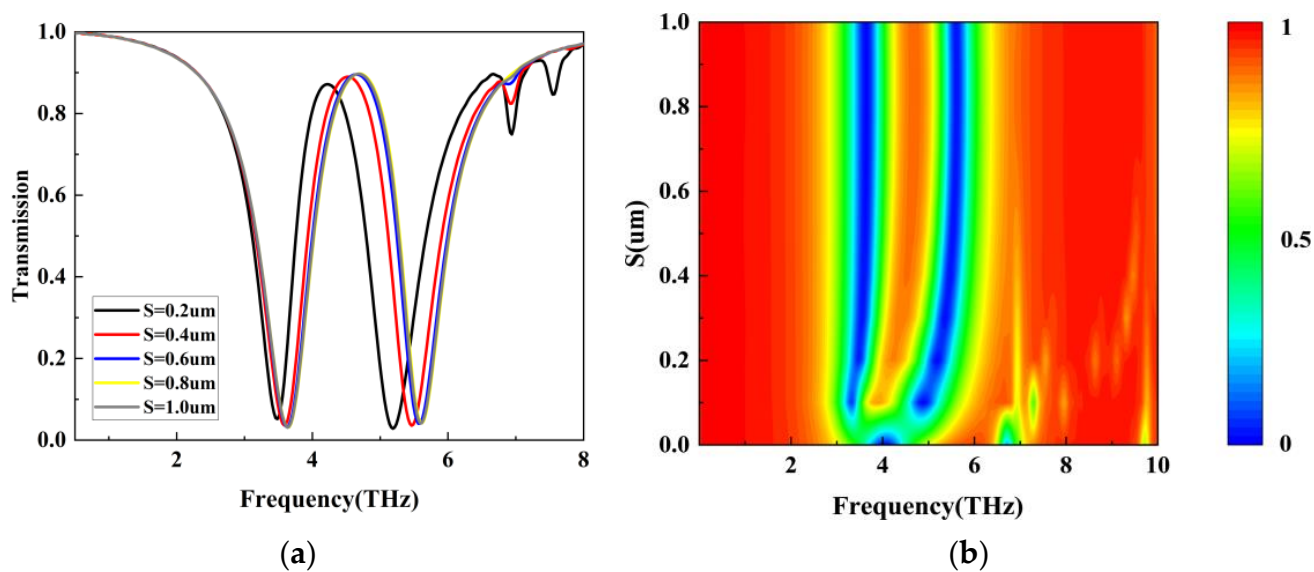
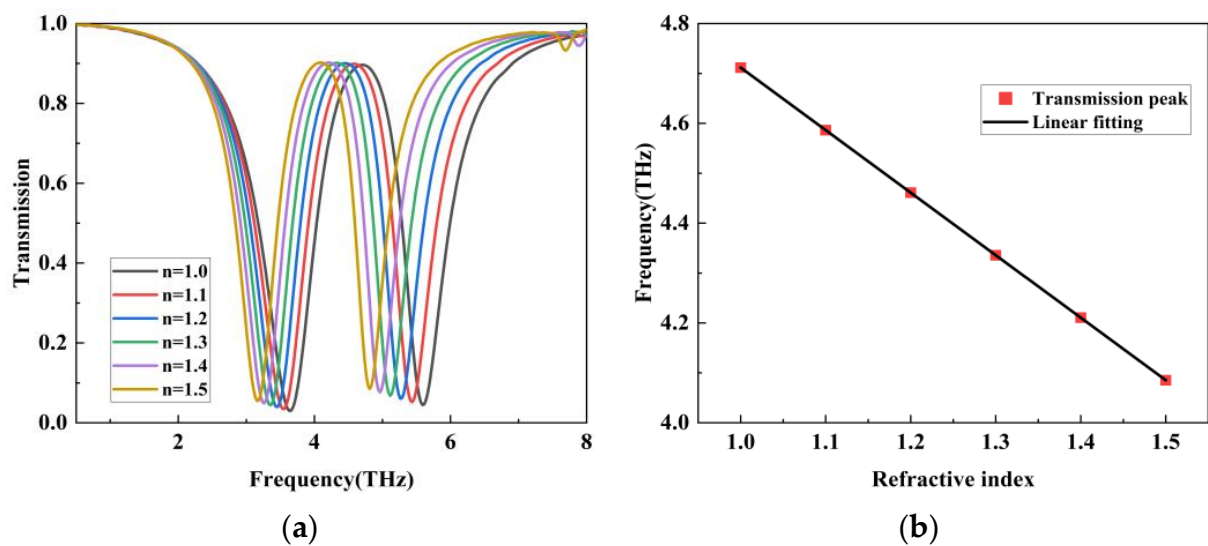


Figure 8. (a) Transmission spectra corresponding to different geometrical parameters  $S$ . (b) Equivalence plots of transmission spectra corresponding to different geometrical parameters  $S$ .

**Table 1.** The transmission curves for different geometrical parameters  $S$  in Figure 8 are fitted with the parameter values obtained from the Lorentzian oscillation coupling model.

$S$ ( $\mu\text{m}$ )	$\omega_1$ (THz)	$\omega_2$ (THz)	$\gamma_1$ (THz)	$\gamma_2$ (THz)	$\tilde{k}$ (THz)
0	6.693	4.079	0.184	0.5736	0.1687
0.1	4.795	3.411	0.5335	0.2457	0.05305
0.2	5.106	3.568	0.4599	0.3245	0.07762
0.3	5.311	3.624	0.4549	0.3491	0.01136
0.4	5.391	3.671	0.3959	0.389	0.0941
0.5	5.415	3.738	0.3777	0.4053	0.2985
0.6	5.5	3.71	0.3673	0.4151	0.1359
0.7	5.499	3.744	0.3593	0.4223	0.2584
0.8	5.5	3.759	0.3554	0.4258	0.2941
0.9	5.485	3.774	0.3547	0.4265	0.3357
1.0	5.5	3.743	0.3594	0.4222	0.2549



**Figure 9.** (a) Transmission spectra with different refractive indices. (b) Fitted curves between transmission peaks and refractive indices.

**Table 2.** Comparison between the proposed PIT graphene metamaterial and previous work.

Structure	Metamaterial	Working Band	Sensitivity (THz/RIU)	Active Tunability	Ref.
Strip	Al	0.60–2.00	0.31	None	[17]
Strip	Graphene	1.00–6.00	0.36	Electric-tuning	[50]
U-shaped & Strip	Au-Graphene	0.30–1.80	0.44	Electric-tuning	[51]
Ring & strip	Graphene	2.00–5.00	1.00	Electric-tuning	[39]
Strip & H-shaped	Graphene	0.50–1.00	/	Electric-tuning	[52]
Ring & Split-ring	Graphene	1.00–4.00	1.10	Electric-tuning	[53]
Strip	Graphene	0.50–8.00	1.25	Electric-tuning	This work

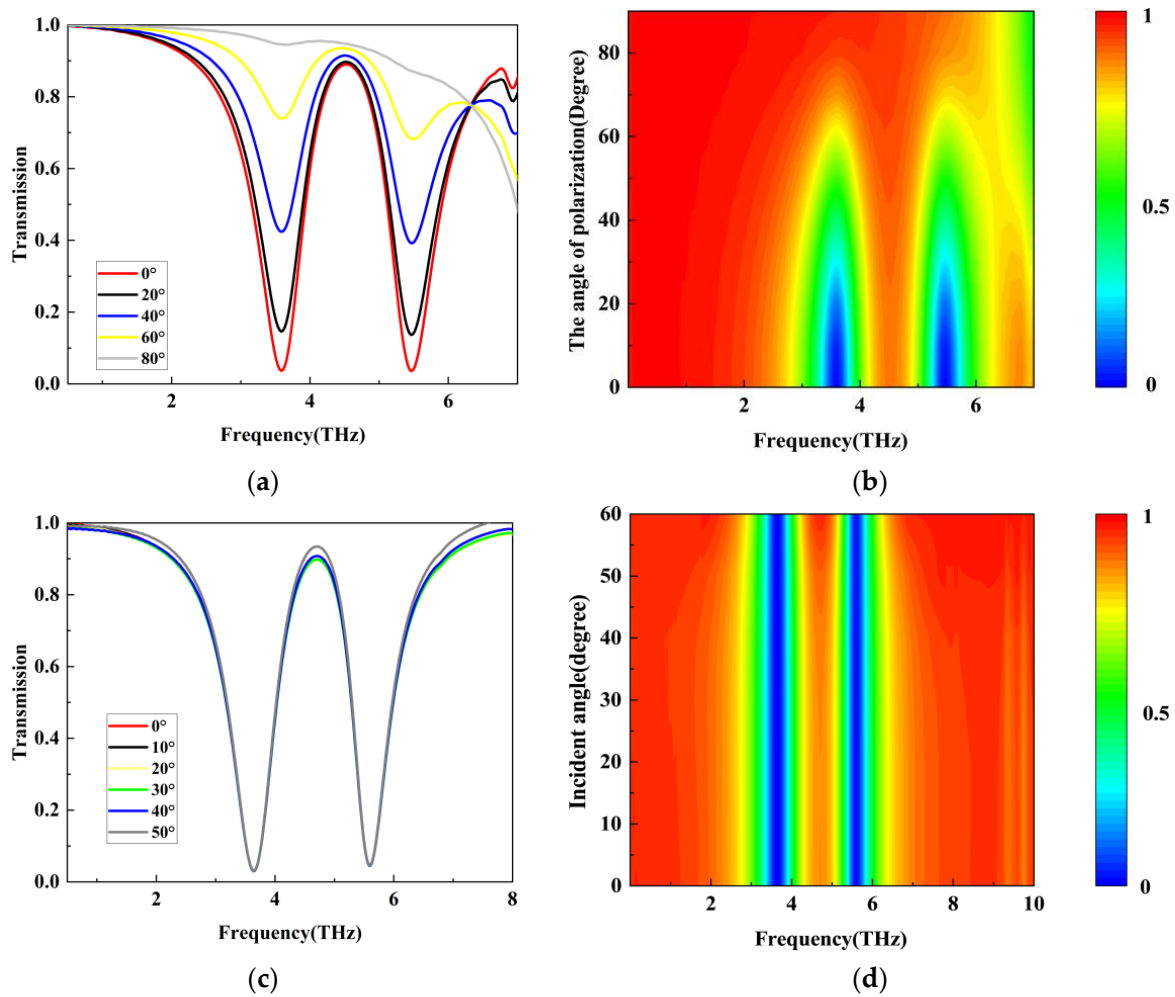


**Figure 10.** (a) Transmission spectra of different polarization angles. (b) Equivalence plots of transmission spectra corresponding to different polarization angles. (c) Transmission spectra of different incidence angles. (d) Equivalence plots of transmission spectra corresponding to different incidence angles.

#### 4. Conclusions

In summary, this work presents a numerical and theoretical study of a PIT system based on bright–bright mode-coupled graphene metamaterials. Both graphene bands act as bright modes, and a PIT window appears due to the weak hybridization between them. The analysis of the chemical potential and carrier mobility of graphene as well as the geometrical parameters of the structure shows that these parameters can modulate the resonant frequency and resonant intensity of the PIT window. Meanwhile, the Lorentzian oscillation coupling mode is fitted to the simulation results of the proposed structure by the finite difference in time domain (FDTD) method, and the simulation results are in good agreement with the Lorentzian coupling model curves. It is noteworthy that when the chemical potential of graphene is changed, the PIT window is blue-shifted, and the modulation depths of transmission peaks and transmission valleys reach 96.14%, 92.39%, and 90.4%, respectively. The damping factors  $\gamma_1$  and  $\gamma_2$  reach 0.36 THz and 0.42 THz, respectively. They are stabilized when the distance between two parallel graphene strips is greater than 0.6  $\mu\text{m}$ . Furthermore, due to its dispersive properties, the realized PIT window has a sensitive response to the surrounding medium up to 1.25 THz/RIU. This PIT effect-based graphene structure has important implications for the future design of terahertz modulators, optical switches, and ultrasensitive sensors.

**Author Contributions:** Conceptualization and model, A.Z.; numerical simulation, A.Z. and P.B.; writing—original draft preparation, A.Z. and P.B.; investigation and formal analysis C.H.; writing—review and editing, A.Z., P.B. and L.C.; project administration and resources, R.M. All authors have read and agreed to the published version of the manuscript.

**Funding:** This work is partially funded by the National Natural Science Foundation of China (62161008), the Guangxi Natural Science Foundation Joint Funding Project (2018GXNSFAA138115), Guangxi Key Laboratory of Automatic Detecting Technology and Instruments (YQ22110), the Open Project Program of Shanxi Key Laboratory of Advanced Semiconductor Optoelectronic Devices and Integrated Systems (No. 2023SZKF04, No. 2023SZKF10), Shanxi Province Science and Technology Major Program (No. 202201030201009).

**Institutional Review Board Statement:** Not applicable.

**Informed Consent Statement:** Not applicable.

**Data Availability Statement:** The data supporting the findings of this study are available within the article.

**Conflicts of Interest:** The authors declare no conflict of interest.

## References

1. Fleischhauer, M.; Imamoglu, A.; Marangos, J.P. Electromagnetically induced transparency: Optics in coherent media. *Rev. Mod. Phys.* **2005**, *77*, 633–673. [[CrossRef](#)]
2. Taubert, R.; Hentschel, M.; Giessen, H. Plasmonic analog of electromagnetically induced absorp-tion: Simulations, experiments, and coupled oscillator analysis. *J. Opt. Soc. Am. B* **2013**, *30*, 3123. [[CrossRef](#)]
3. Papanikolaou, N.; Fu, Y.H.; Fedotov, V.A.; Prosvirnin, S.L.; Tsai, D.P.; Zheludev, N.I. Metamaterial with polarization and direction insensitive resonant transmission response mimicking electromagnetically induced transparency. *Appl. Phys. Lett.* **2009**, *94*, 211902. [[CrossRef](#)]
4. Shamshirband, S.; Malvandi, A.; Karimipour, A.; Goodarzi, M.; Afrand, M.; Petković, D.; Dahari, M.; Mahmoodian, N. Performance investigation of micro- and nano-sized particle erosion in a 90° elbow using an ANFIS model. *Powder Technol.* **2015**, *284*, 336–343. [[CrossRef](#)]
5. Noh, S.M.C.; Shamshirband, S.; Petković, D.; Penny, R.; Zakaria, R. Adaptive neuro-fuzzy appraisal of plasmonic studies on morphology of deposited silver thin films having different thicknesses. *Plasmonics* **2014**, *9*, 1189–1196. [[CrossRef](#)]
6. Zakaria, R.; Noh, S.M.C.; Petković, D.; Shamshirband, S.; Penny, R. RETRACTED: Investigation of plasmonic studies on morphology of deposited silver thin films having different thicknesses by soft computing methodologies—A comparative study. *Phys. E Low-Dimens. Syst. Nanostructures* **2014**, *63*, 317–323. [[CrossRef](#)]
7. Zhang, S.; Genov, D.A.; Wang, Y.; Liu, M.; Zhang, X. Plasmon-Induced transparency in metamaterials. *Phys. Rev. Lett.* **2008**, *101*, 047401. [[CrossRef](#)]
8. Liu, N.; Weiss, T.; Mesch, M.; Langguth, L.; Eigenthaler, U.; Hirscher, M.; Sönnichsen, C.; Giessen, H. Planar metamaterial analogue of electromagnetically induced transparency for plasmonic sensing. *Nano Lett.* **2009**, *10*, 1103–1107. [[CrossRef](#)]
9. Yang, Y.; Kravchenko, I.I.; Briggs, D.P.; Valentine, J. All-dielectric metasurface analogue of electromagnetically induced transparency. *Nat. Commun.* **2014**, *5*, 5753. [[CrossRef](#)]
10. Han, S.; Singh, R.; Cong, L.; Yang, H. Engineering the fano resonance and electromagnetically induced transparency in near-field coupled bright and dark metamaterial. *J. Phys. D Appl. Phys.* **2014**, *48*, 035104. [[CrossRef](#)]
11. Wei, Z.; Li, X.; Zhong, N.; Tan, X.; Zhang, X.; Liu, H.; Meng, H.; Liang, R. Analogue Electromagnetically Induced Transparency Based on Low-loss Metamaterial and its Application in Nanosensor and Slow-light Device. *Plasmonics* **2016**, *12*, 641–647. [[CrossRef](#)]
12. Fu, G.-L.; Zhai, X.; Li, H.-J.; Xia, S.-X.; Wang, L.-L. Tunable plasmon-induced transparency based on bright-bright mode coupling between two parallel graphene nanostrips. *Plasmonics* **2016**, *11*, 1597–1602. [[CrossRef](#)]
13. Jin, X.-R.; Park, J.; Zheng, H.; Lee, S.; Lee, Y.; Rhee, J.Y.; Kim, K.W.; Cheong, H.S.; Jang, W.H. Highly-dispersive transparency at optical frequencies in planar metamaterials based on two-bright-mode coupling. *Opt. Express* **2011**, *19*, 21652. [[CrossRef](#)] [[PubMed](#)]
14. Ding, G.-W.; Liu, S.-B.; Zhang, H.-F.; Kong, X.-K.; Li, H.-M.; Li, B.-X.; Liu, S.-Y.; Li, H. Tunable electromagnetically induced transparency at terahertz frequencies in coupled graphene metamaterial. *Chin. Phys. B* **2015**, *24*, 118103. [[CrossRef](#)]
15. Hu, X.; Yuan, S.; Armghan, A.; Liu, Y.; Jiao, Z.; Lv, H.; Zeng, C.; Huang, Y.; Huang, Q.; Wang, Y.; et al. Plasmon induced transparency and absorption in bright–bright mode coupling metamaterials: A radiating two-oscillator model analysis. *J. Phys. D Appl. Phys.* **2016**, *50*, 025301. [[CrossRef](#)]
16. Zhang, H.; Cao, Y.; Liu, Y.; Li, Y.; Zhang, Y. A novel graphene metamaterial design for tunable terahertz plasmon induced transparency by two bright mode coupling. *Opt. Commun.* **2017**, *391*, 9–15. [[CrossRef](#)]

17. Chen, M.; Singh, L.; Xu, N.; Singh, R.; Zhang, W.; Xie, L. Terahertz sensing of highly absorptive water-methanol mixtures with multiple resonances in metamaterials. *Opt. Express* **2017**, *25*, 14089. [[CrossRef](#)] [[PubMed](#)]
18. Pan, W.; Yan, Y.; Ma, Y.; Shen, D. A terahertz metamaterial based on electromagnetically induced transparency effect and its sensing performance. *Opt. Commun.* **2019**, *431*, 115–119. [[CrossRef](#)]
19. Fang, Z.; Pan, C.; Xue, Y.; Wu, B.; Wu, E. Polarization control of plasmon-induced transparency in metamaterials with reversibly convertible bright and dark modes. *Appl. Opt.* **2021**, *60*, 10689. [[CrossRef](#)]
20. Wang, X.; Chen, C.; Gao, P.; Dai, Y.; Zhao, J.; Lu, X.; Wan, Y.; Zhao, S.; Liu, H. Slow-Light and sensing performance analysis based on plasmon-induced transparency in terahertz graphene metasurface. *IEEE Sens. J.* **2023**, *23*, 4794–4801. [[CrossRef](#)]
21. Xiao, G.; Zhou, S.; Yang, H.; Lin, Z.; Li, H.; Liu, X.; Chen, Z.; Sun, T.; Wangyang, P.; Li, J. Dynamically tunable and multifunctional polarization beam splitters based on graphene metasurfaces. *Nanomaterials* **2022**, *12*, 3022. [[CrossRef](#)] [[PubMed](#)]
22. Wang, Z.; Xu, Y.; Chen, F.; Cheng, S.; Yi, Z.; Xiao, G.; Li, Y.; Jiang, J.; Zhou, X.; Chen, Z. Tunable multi-narrowband perfect absorber based on graphene and black phosphorus metamaterial. *Optik* **2022**, *270*, 169932. [[CrossRef](#)]
23. Hong, Q.; Xiong, F.; Xu, W.; Zhu, Z.; Liu, K.; Yuan, X.; Zhang, J.; Qin, S. Towards high performance hybrid two-dimensional material plasmonic devices: Strong and highly anisotropic plasmonic resonances in nanostructured graphene-black phosphorus bilayer. *Opt. Express* **2018**, *26*, 22528. [[CrossRef](#)] [[PubMed](#)]
24. Nong, J.; Tang, L.; Lan, G.; Luo, P.; Guo, C.; Yi, J.; Wei, W. Wideband tunable perfect absorption of graphene plasmons via attenuated total reflection in Otto prism configuration. *Nanophotonics* **2020**, *9*, 645–655. [[CrossRef](#)]
25. Nong, J.; Tang, L.; Lan, G.; Luo, P.; Li, Z.; Huang, D.; Yi, J.; Shi, H.; Wei, W. Enhanced graphene plasmonic mode energy for highly sensitive molecular fingerprint retrieval. *Laser Photonics Rev.* **2020**, *15*, 2000300. [[CrossRef](#)]
26. Zhou, X.; Xu, Y.; Li, Y.; Cheng, S.; Yi, Z.; Xiao, G.; Wang, Z.; Chen, Z. Multi-frequency switch and excellent slow light based on tunable triple plasmon-induced transparency in bilayer graphene metamaterial. *Commun. Theor. Phys.* **2022**, *74*, 115501. [[CrossRef](#)]
27. Xia, S.; Zhai, X.; Wang, L.; Wen, S. Plasmonically induced transparency in in-plane isotropic and anisotropic 2D materials. *Opt. Express* **2020**, *28*, 7980. [[CrossRef](#)]
28. Nong, J.; Tang, L.; Lan, G.; Luo, P.; Li, Z.; Huang, D.; Shen, J.; Wei, W. Combined visible plasmons of Ag nanoparticles and infrared plasmons of graphene nanoribbons for high-performance surface-enhanced Raman and infrared spectroscopies. *Small* **2020**, *17*, 2004640. [[CrossRef](#)]
29. Nong, J.; Wei, W.; Lan, G.; Luo, P.; Guo, C.; Yi, J.; Tang, L. Resolved infrared spectroscopy of aqueous molecules employing tunable graphene plasmons in an Otto prism. *Anal. Chem.* **2020**, *92*, 15370–15378. [[CrossRef](#)]
30. Yu, A.; Guo, X.; Zhu, Y.; Balakin, A.V.; Shkurinov, A.P. Metal-graphene hybridized plasmon induced transparency in the terahertz frequencies. *Opt. Express* **2019**, *27*, 34731. [[CrossRef](#)]
31. Dong, Z.; Sun, C.; Si, J.; Deng, X. Tunable polarization-independent plasmonically induced transparency based on metal-graphene metasurface. *Opt. Express* **2017**, *25*, 12251. [[CrossRef](#)] [[PubMed](#)]
32. Zhang, T.; Liu, Q.; Dan, Y.; Yu, S.; Han, X.; Dai, J.; Xu, K. Machine learning and evolutionary algorithm studies of graphene metamaterials for optimized plasmon-induced transparency. *Opt. Express* **2020**, *28*, 18899. [[CrossRef](#)] [[PubMed](#)]
33. Zhou, F.; Wang, Y.; Zhang, X.; Wang, J.; Liu, Z.; Luo, X.; Zhang, Z.; Gao, E. Dynamically adjustable plasmon-induced transparency and switching application based on bilayer graphene metamaterials. *J. Phys. D Appl. Phys.* **2020**, *54*, 054002. [[CrossRef](#)]
34. Feng, Y.; Li, Z.; Zhao, Q.; Chen, P.; Wang, J. Evaluation of Fano resonance and phase analysis of plasma induced transparency in photonic nanostructure based on equivalent circuit analysis. *J. Opt.* **2022**, *24*, 035001. [[CrossRef](#)]
35. Xiao, B.; Tong, S.; Fyffe, A.; Shi, Z. Tunable electromagnetically induced transparency based on graphene metamaterials. *Opt. Express* **2020**, *28*, 4048. [[CrossRef](#)]
36. Gao, E.; Li, H.; Liu, Z.; Xiong, C.; Liu, C.; Ruan, B.; Li, M.; Zhang, B. Terahertz multifunction switch and optical storage based on triple plasmon-induced transparency on a single-layer patterned graphene metasurface. *Opt. Express* **2020**, *28*, 40013. [[CrossRef](#)]
37. Xu, H.; Li, M.; Chen, Z.; He, L.; Dong, Y.; Li, X.; Wang, X.; Nie, G.; He, Z.; Zeng, B. Optical tunable multifunctional applications based on graphene metasurface in terahertz. *Phys. Scripta.* **2023**, *98*, 045511. [[CrossRef](#)]
38. Zhou, X.; Xu, Y.; Li, Y.; Cheng, S.; Yi, Z.; Xiao, G.; Wang, Z.; Chen, Z. High-sensitive refractive index sensing and excellent slow light based on tunable triple plasmon-induced transparency in monolayer graphene based metamaterial. *Commun. Theor. Phys.* **2022**, *75*, 015501. [[CrossRef](#)]
39. Ge, J.; You, C.; Feng, H.; Li, X.; Wang, M.; Dong, L.; Veronis, G.; Yun, M. Tunable dual plasmon-induced transparency based on a monolayer graphene metamaterial and its terahertz sensing performance. *Opt. Express* **2020**, *28*, 31781. [[CrossRef](#)]
40. Yang, G.; Liu, Z.; Zhou, F.; Zhuo, S.; Qin, Y.; Luo, X.; Ji, C.; Xie, Y.; Yang, R. Effect of symmetry breaking on multi-plasmon-induced transparency based on single-layer graphene metamaterials with strips and rings. *J. Opt. Soc. Am. A* **2023**, *40*, 841. [[CrossRef](#)]
41. Gu, X.; Zhang, H.-F.; Li, M.-Y.; Chen, J.-Y.; He, Y. Theoretical analysis of tunable double plasmon induced transparency in three-ellipse-shaped resonator coupled waveguide. *Acta Phys. Sin.* **2022**, *71*, 247301. [[CrossRef](#)]
42. Zhu, A.; Bu, P.; Hu, C.; Niu, J.; Mahapatra, R. High extinction ratio  $4 \times 2$  encoder based on electro-optical graphene plasma structure. *Photonics* **2023**, *10*, 216. [[CrossRef](#)]
43. Xu, H.; Zhao, M.; Zheng, M.; Xiong, C.; Zhang, B.; Peng, Y.; Li, H. Dual plasmon-induced transparency and slow light effect in monolayer graphene structure with rectangular defects. *J. Phys. D Appl. Phys.* **2018**, *52*, 025104. [[CrossRef](#)]

44. Zhao, M.; Xu, H.; Xiong, C.; Zhang, B.; Liu, C.; Xie, W.; Li, H. Tunable slow light effect based on dual plasmon induced transparency in terahertz planar patterned graphene structure. *Results Phys.* **2019**, *15*, 102796. [[CrossRef](#)]
45. Gan, C.H.; Chu, H.S.; Li, E.P. Synthesis of highly confined surface plasmon modes with doped graphene sheets in the midinfrared and terahertz frequencies. *Phys. Rev. B* **2012**, *85*, 125431. [[CrossRef](#)]
46. Vakil, A.; Engheta, N. Transformation optics using graphene. *Science* **2011**, *332*, 1291–1294. [[CrossRef](#)] [[PubMed](#)]
47. Chen, M.; Xiao, Z.; Lv, F.; Cui, Z.; Xu, Q. Dynamically tunable electromagnetically induced transparency-like effect in terahertz metamaterial based on graphene cross structures. *IEEE J. Sel. Top. Quantum Electron.* **2022**, *28*, 1–9. [[CrossRef](#)]
48. Tang, B.; Jia, Z.; Huang, L.; Su, J.; Jiang, C. Polarization-Controlled dynamically tunable electromagnetically induced transparency-like effect based on graphene metasurfaces. *IEEE J. Sel. Top. Quantum Electron.* **2021**, *27*, 1–6. [[CrossRef](#)]
49. Ding, J.; Arigong, B.; Ren, H.; Zhou, M.; Shao, J.; Lu, M.; Chai, Y.; Lin, Y.; Zhang, H. Tuneable complementary metamaterial structures based on graphene for single and multiple transparency windows. *Sci. Rep.* **2014**, *4*, 6128. [[CrossRef](#)]
50. Tang, P.; Li, J.; Du, L.; Liu, Q.; Peng, Q.; Zhao, J.; Zhu, B.; Li, Z.; Zhu, L. Ultrasensitive specific terahertz sensor based on tunable plasmon induced transparency of a graphene micro-ribbon array structure. *Opt. Express* **2018**, *26*, 30655. [[CrossRef](#)]
51. Liu, C.; Liu, P.; Yang, C.; Lin, Y.; Zha, S. Dynamic electromagnetically induced transparency based on a metal-graphene hybrid metamaterial. *Opt. Mater. Express* **2018**, *8*, 1132. [[CrossRef](#)]
52. Mei, J.; Shu, C.; Yang, P. Tunable electromagnetically induced transparency in graphene metamaterial in two perpendicular polarization directions. *Appl. Phys. B* **2019**, *125*, 130. [[CrossRef](#)]
53. Chen, T.; Liang, D.; Jiang, W. A tunable terahertz graphene metamaterial sensor based on dual polarized plasmon-induced transparency. *IEEE Sens. J.* **2022**, *22*, 14084–14090. [[CrossRef](#)]

**Disclaimer/Publisher's Note:** The statements, opinions and data contained in all publications are solely those of the individual author(s) and contributor(s) and not of MDPI and/or the editor(s). MDPI and/or the editor(s) disclaim responsibility for any injury to people or property resulting from any ideas, methods, instructions or products referred to in the content.